International Journal of Heat and Fluid Flow 84 (2020) 108620

Contents lists available at ScienceDirect

International Journal of Heat and Fluid Flow

journal homepage: www.elsevier.com/locate/ijhff

Pressure power spectrum in high-Reynolds number wall-bounded flows

Haosen H.A. Xu[a], Aaron Towne[b], Xiang I.A. Yang[*,a], Ivan Marusic[c]

[a] Mechanical Engineering, Penn State University, PA, 16801, USA
[b] Mechanical Engineering, University of Michigan, Ann Arbor, MI, 48109 USA
[c] Department of Mechanical Engineering, University of Melbourne, Victoria 3010, Australia

ARTICLE INFO

Keywords:
Pressure
Boundary layer
Attached eddy hypothesis
Turbulence

ABSTRACT

We study the behaviors of pressure fluctuations in high Reynolds number wall-bounded flows. Pressure fluctuations are small-scale quantities compared to velocity fluctuations in a wall-bounded flow (Tsuji, Marusic, & Johansson, *Int. J. Heat Fluid Flow*, vol. 61, 2016, pp. 2–11.): at a given wall-normal distance y, the premultiplied velocity spectrum peaks at a streamwise wavelength on the order of the boundary layer thickness ($\lambda_x = O(\delta)$), whereas the premultiplied pressure spectrum peaks at $\lambda_x < O(y)$. The differing scales of pressure and velocity pose a challenge to modeling, and the scaling of the pressure spectrum in wall-bounded flows remains an unsolved issue from both a theoretical and measurement standpoint. To address this unresolved issue, we incorporate Kolmogorov's theory (K41) within the framework of Townsend's attached eddy hypothesis to account for the small scale nature of pressure fluctuations, leading to the first derivation that is consistent with both theories. Our main result is that at a wall-normal distance in the logarithmic layer the premultiplied pressure power spectrum scales as $[k_x E_{pp}] \sim \lambda_x^{n-1} y^{-(3+n)/4}$, for $\lambda_x < y/\tan(\theta)$, and as $[k_x E_{pp}] \sim \lambda_x^{(3n-7)/4}$, for $\lambda_x > y/\tan(\theta)$. Here, θ is the attached-eddy inclination angle, k_x is the streamwise wavenumber, the velocity spectrum follows a k^{-1} scaling for $1/k_x > y/tan(\theta)$ and a $k^{-5/3}$ scaling for $1/k_x < y/\tan(\theta)$, and n is a Reynolds-number-dependent constant. This result conforms to Kolmogorov's theory of small scale turbulence, i.e., it yields a $-7/3$ scaling for the small scales at high Reynolds numbers, and also yields the anticipated -1 scaling for the logarithmic layer scales. Detailed analysis shows that pressure and spanwise velocity have differently statistical properties: while an outer peak emerges in the premultiplied spanwise velocity spectrum at high Reynolds numbers, no outer peak is expected in the premultiplied pressure spectrum. The derived scalings are confirmed using data from a direct numerical simulation of a channel flow at friction Reynolds number $Re_\tau = 5200$.

1. Introduction

Pressure is an important flow quantity for many engineering and environmental flow applications, including vibration and fatigue. According to Kolmogorov's theory of small-scale turbulence (Kolmogorov, 1941; Obukhov, 1949; Corrsin, 1951), the pressure power spectrum scales as $E_{pp} \sim k^{-7/3}$ in the inertial range. Evidence of this $-7/3$ scaling was later found in, e.g., Gotoh and Fukayama (2001) and Tsuji and Ishihara (2003), in the context of isotropic turbulence at Taylor microscale Reynolds number $Re_\lambda > 600$. Predicting pressure statistics in the context of wall-bounded flows is more difficult, and the scaling of the pressure spectrum is an unresolved issue from a theoretical standpoint.

Directly measuring pressure fluctuations in a laboratory experiment is challenging (Lauchle and Daniels, 1987; Tsuji et al., 2012), as pressure signals in wind tunnels are contaminated by noise from the tunnel fan and flow in the return circuit. Tsuji et al. (2012) compared laboratory measurements and direct numerical simulation (DNS) data and concluded that background noise in wind tunnels affect the pressure in the boundary layer, which in turn result in pressure profiles that are different from DNS. Having this caveat in mind, laboratory measurements of Elliott (1972) and Albertson et al. (1998) suggest a -1.7 scaling and a -1.5 scaling, respectively, instead of the expected $-7/3$ scaling. Because the small scales are approximately isotropic at high Reynolds numbers, in general, we expect Kolmogorov's theory to be valid at small scales even for flows with mean shear (Pope, 2001).

Compared to laboratory experiments (Tsuji et al., 2005; Liu and Katz, 2006; Tsuji, 2007), getting pressure data from numerical simulations, e.g., DNS, is much more straightforward. For example, Kim (1989) and Abe et al. (2005) divided the pressure source term into a rapid part and a slow part and found that the slow pressure fluctuations are dominant in the channel except very near the wall.

* Corresponding author.
E-mail address: xzy48@psu.edu (X.I.A. Yang).

https://doi.org/10.1016/j.ijheatfluidflow.2020.108620
Received 30 January 2020; Received in revised form 1 April 2020; Accepted 23 April 2020

Patwardhan and Ramesh (2014) found in a DNS boundary layer flow that the pressure spectrum follows a -1 scaling near the wall (Bradshaw, 1967) and a $-7/3$ scaling in the outer region. In a recent work, Panton et al. (2017) found that

$$\langle p'p' \rangle \sim \log(\delta/y) \tag{1}$$

in the logarithmic layer, where δ is the half-channel width, $'$ indicates the fluctuation from the mean, and $< \cdot >$ is the ensemble average.

A similar logarithmic scaling was previously found for the streamwise velocity variance (Smits et al., 2011; Marusic et al., 2013), i.e.,

$$\langle u'u' \rangle \sim \log(\delta/y), \tag{2}$$

whose presence in high Reynolds number wall-bounded flows was predicted by Townsend as a result of his attached eddy hypothesis (AEH) (Townsend, 1976; Woodcock and Marusic, 2015; Yang and Abkar, 2018; Marusic and Monty, 2019). Despite their similar forms, the two scalings in Eqs. (1) and (2) are due to eddies at different scales, as pointed out by Tsuji et al. (2016). In their recent work, Tsuji et al. (2016) divided the instantaneous pressure into a large-scale component p_L and a small scale component p_S based on a cutoff length scale λ_c. They examined $\langle p_L^2 \rangle$ and $\langle p_S^2 \rangle$ and concluded that the logarithmic scaling in Eq. (1) is due to the smaller scales ($\lambda_x \ll c\delta$), in contrast to the logarithmic scaling in Eq. (2), which is due to the larger scales ($\lambda_x > c\delta$). Here, λ_x is the streamwise wavelength, c is a constant (Christensen and Adrian, 2001; Marusic and Heuer, 2007).

Here, we examine the pressure and velocity spectra at a wall-normal distance where Eq. (1) is valid, i.e., in the logarithmic layer. This will give us a better idea of the scales that dominate velocity and pressure fluctuations. Fig. 1(a) shows the compensated pressure variance, i.e.,

$$\text{err} = \langle p'p' \rangle - A_p \log(\delta/y) - B_p, \tag{3}$$

in a $Re_\tau = 5200$ channel (Lee and Moser, 2015), where $A_p = 2.6$ and $B_p = .24$. The DNS computational domain is $8\pi\delta \times 2\delta \times 3\pi\delta$. The grid resolution is $\Delta x^+ \times \Delta y^+ \times \Delta z^+ = 12.7 \times 6.4 \times 10.4$ at the centerline and is $\Delta y^+ = 0.071$ at the wall. Further details of the DNS can be found in

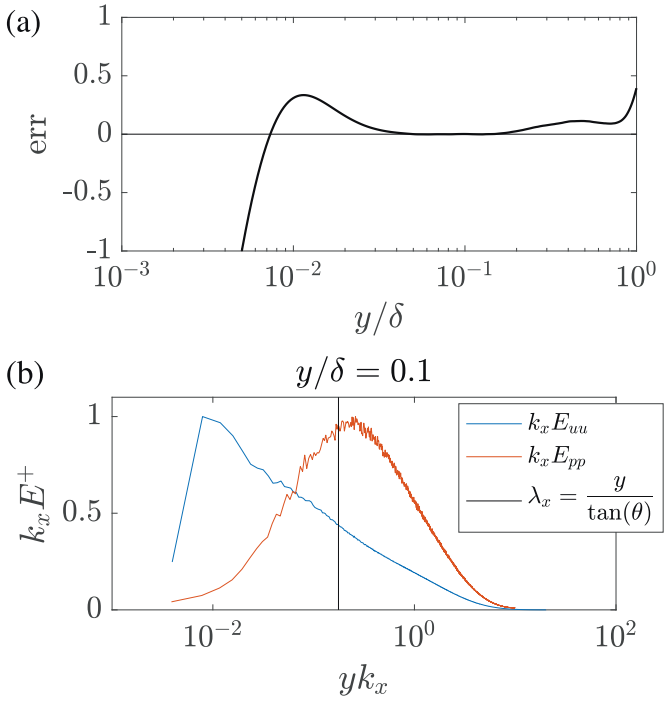

Fig. 1. (a) err $= \langle p'p' \rangle - A_p \log(\delta/y) - B_p$ as a function of the wall-normal distance in a $Re_\tau = 5200$ channel (Lee and Moser, 2015). (b) The premultiplied velocity and pressure power spectra. The spectra are normalized with their peak values.

Kim et al. (1987), Lee and Moser (2015), and Graham et al. (2016). According to Fig. 1(a), the variance of the pressure fluctuations follows a logarithmic scaling near $y/\delta = 0.1$. Fig. 1(b) shows the premultiplied velocity and pressure spectra as a function of the streamwise wavenumber at the wall-normal height. It is clear that velocity fluctuations are most energetic at large scales whereas pressure fluctuations are most energetic at small scales. Specifically, as will become clear in the later sections, pressure fluctuations are most energetic at scales $\lambda_x < y/\tan(\theta)$, and velocity fluctuations are most energetic at scales $y/\tan(\theta) < \lambda_x$ (Hu et al., 2020). The differing scales of velocity and pressure fluctuations pose challenge to modeling. Specifically, AEH, which has been quite useful in providing scaling estimates of velocity statistics in high Reynolds number wall-bounded flows, is a model of the large-scale energetic motions not the small scales, and therefore, it does not directly provide scaling estimates for pressure power spectra.

In summary, the scaling of the pressure spectrum in wall-bounded flows is an unsolved problem from both a theoretical and measurement standpoint. The objective of this work is to address this unresolved issue. We do this by combining AEH and K41 to model pressure and velocity fluctuations in a unified framework. In addition to the pressure power spectrum, we will also explore the scaling of other pressure statistics. The rest of the paper is organized as follows. In Section 2, we review the basics of K41 and its estimates of pressure statistics for isotropic turbulence. In Section 3, we combine AEH and K41 and make estimates of pressure statistics in wall-bounded flows. The data are compared to our model in Section 4. We further extend the model in Sections 5 and 6. Concluding remarks are presented in Section 7.

2. Background knowledge

We begin by reviewing the basics of K41 and AEH, which serve as building blocks for the pressure model developed later in Section 3.

2.1. Kolmogorov's theory of small scale turbulence

K41 essentially models the behavior of the small scale turbulence, at which scales the flow is approximately homogeneous and isotropic. Here, let us consider an isotropic turbulent "eddy". Here and throughout this paper, an "eddy" is not necessarily an energetic fluid motion at a particular scale; rather, an "eddy" is a flow structure across a range of scales. This isotropic turbulent "eddy" has a characteristic velocity u, and an integral length scale l. The fluid viscosity is ν and the fluid density is unit (i.e., $\rho \equiv 1$). Dissipation in this eddy is

$$\epsilon \sim \frac{\text{Characteristic velocity}^3}{\text{Characteristic length}} \sim \frac{u^3}{l}. \tag{4}$$

At high Reynolds numbers, the dissipation ϵ and the eddy size l, equivalently the characteristic velocity u and the eddy size l, determine the state of the eddy. Dimensional analysis gives estimates of all flow statistics in terms of these two quantities at scales away from the Kolmogorov length and the integral length scale. In the following, we highlight a few of these estimates. The variance of the pressure fluctuation is

$$\langle p'^2 \rangle \sim [U]^4 \sim (\epsilon l)^{4/3} \sim u^4, \tag{5}$$

where $< \cdot >$ is the ensemble average of the quantity in the bracket, and $[U]$ denotes the dimension of velocities, i.e., [m/s]. The power spectrum of the pressure fluctuation scales as

$$E_{pp} \sim [U]^4 [L] \sim \epsilon^{4/3} k^{-7/3} \sim \frac{u^3}{l} k^{-7/3}, \tag{6}$$

where $[L]$ denotes the dimension of lengths, i.e., [m], and k is the wavenumber. The $-7/3$ law in Eq. (6) is only found at high Reynolds numbers, i.e., $Re_\lambda > O(600)$ (Tsuji and Ishihara, 2003). Detailed analysis shows that

$$E_{pp} = K_p \epsilon^{3/4} \nu^{7/4} (k\eta)^{-n} = K_p \epsilon^{(3+n)/4} \nu^{(7-3n)/4} k^{-n}, \tag{7}$$

in finite Reynolds number isotropic turbulence (Tsuji and Ishihara, 2003). Here, K_p is a constant, η is the Kolmogorov length scale, and n is the power exponent. The exact value of n depends on the Reynolds number, i.e., Re_λ (Cao et al., 1999; Vedula and Yeung, 1999).

2.2. Attached eddy hypothesis

AEH models high-Reynolds number boundary-layer flows as assemblies of self-similar wall-attached eddies. The characteristic velocity scale of an attached eddy is

$$\begin{aligned}&\text{characteristic velocity scale of an attached eddy}\\ &= \sqrt{\text{momentum flux carried by the eddy}} = u_\tau,\end{aligned} \tag{8}$$

and all the eddies are self-similar. The size of a wall-attached eddy at a distance y from the wall is $l_y \sim y$, and it follows that the eddy population density is

$$\rho_N \sim \frac{1}{l_y} \sim \frac{1}{y}. \tag{9}$$

According to AEH, a flow quantity at a wall-normal height y can be computed by adding up contributions from wall-attached eddies above that height (Yang et al., 2016; Yang and Abkar, 2018):

$$\begin{aligned}&[\text{a flow quantity}]\\ &= \int_y^\delta [\text{contribution from a } y'\text{-sized eddy}]\\ &\quad \times [\text{eddy population density}]\, dy'.\end{aligned} \tag{10}$$

3. Model

Let us now consider a y'-sized attached eddy in a high Reynolds number wall-bounded turbulent flow. This eddy is a turbulent eddy. According to our definition, a turbulent eddy has energy in many scales. Velocity fluctuations are most energetic at large scales, which are modeled by AEH, and pressure fluctuations are most energetic at small scales, which are modeled by K41. The small scales have an integral length scale on the order of $O(y')$ and a characteristic velocity scale of $O(u_\tau)$. The objective here is to make use of AEH and K41 to estimate pressure statistics in boundary-layer flows.

3.1. Dissipation

Before considering pressure, we first estimate dissipation statistics in a boundary layer, which will be needed later to obtain our model for pressure. Each attached eddy dissipates some turbulent kinetic energy, and Eq. (10) applies. We have

$$\begin{aligned}\epsilon(y) = \int_y^\delta &[\text{dissipation of a } y'\text{-sized attached eddy}]\\ &\times [\text{eddy population density}]\, dy'.\end{aligned} \tag{11}$$

AEH itself does not give an estimate of the [dissipation of a y'-sized attached eddy]. Nevertheless, that estimate can be obtained from K41, and Eqs. (4) and (8) give

$$[\text{dissipation of a } y'\text{-sized attached eddy}] \sim \frac{u_\tau^3}{y'}. \tag{12}$$

Plugging Eqs. (9) and (12) into Eq. (11), we have

$$\epsilon(y) \sim \int_y^\delta \frac{u_\tau^3}{y'} \frac{1}{y'} dy' \sim \frac{u_\tau^3}{y}, \quad 1 \ll y^+ \ll \delta^+. \tag{13}$$

Eq. (13) serves as a consistency check for Eq. (10) because $\epsilon(y) \approx P(y) = -\langle u'v' \rangle dU/dy = u_\tau^3/\kappa y$ in the logarithmic layer (Jiménez, 2012).

3.2. Pressure fluctuations

3.2.1. Pressure variance

Following the discussion in the above sections, we estimate pressure statistics in a boundary layer. Applying Eq. (10) to estimate pressure variance, we have

$$\begin{aligned}&\langle p'p' \rangle\\ &= \int_y^\delta [\text{pressure variance due to a } y'\text{-sized attached eddy}]\\ &\quad \times [\text{eddy population density}]\, dy'.\end{aligned} \tag{14}$$

Pressure is most energetic at scales where $E_{uu} \sim k^{-5/3}$, and AEH itself does not provide an estimates of motions at those scales. Following the discussion in the previous subsection, we resort to K41 for an estimates of [pressure variance of a y' -sized attached eddy]: Eqs. (5) and (8) give

$$\begin{aligned}&[\text{pressure variance of a } y'\text{-sized attached eddy}]\\ &\sim u_\tau^4,\end{aligned} \tag{15}$$

Plugging Eqs. (15) and (9) into Eq. (14), we have

$$\langle p'p' \rangle \sim \int_y^\delta u_\tau^4 \frac{1}{y'}\, dy' \sim \log(\delta/y), \tag{16}$$

leading to the logarithmic scaling in Eq. (1). To the best of our knowledge, this is the first derivation for the scaling $< p'p' > \sim \log(\delta/y)$ that acknowledge the fact that pressure is a small-scale quantity and is consistent with the attached eddy hypothesis. We make an observation: according to Eq. (15), pressure variance due to a y'-sized eddy does not depend on y'. We will make use of this observation in Section 5.

3.2.2. Pressure spectrum

In this section, we estimate the scaling of the pressure spectrum. First, we estimate [the premultiplied pressure and velocity spectrum due to y'-sized attached eddies]. Following our discussion in Section 1, we divide the energy content of an attached eddy to a large-scale part, i.e., $y/\tan(\theta) < \lambda_x < c\delta$ and a small-scale part, i.e., $\lambda_x < y/\tan(\theta)$, as sketched in Fig. 2(a). Here $\lambda_x = c\delta$ is the location of the outer peak. The scale cutoff that separates the small and the large scales is defined based on the eddy inclination angle. This definition naturally follows from Townsend's attached eddy hypothesis. For this discussion, the cutoff should be such that the velocity spectrum follows a k^{-1} scaling above the cutoff and a $k^{-5/3}$ scaling below the cutoff. Like the eddy inclination angle, this definition also allows for some arbitrariness: after all, the transition from the -1 scaling to the $-5/3$ scaling does not happen at a particular scale but across many scales. In the following section (particularly from Fig. 4), we will see that the scale cutoff could be defined anywhere between $2y$ to $6y$ without affecting our conclusions. Velocity fluctuations are most energetic at the large scales, and pressure fluctuations are most energetic at the small scales. Hereon, for simplicity, we neglect contributions from the small scales to the premultiplied velocity spectrum and contributions from the large scales to the premultiplied pressure spectrum. Because of the random repetitions of the y'-size attached eddies in space, the premultiplied velocity spectrum due to y'-sized eddies, which measures the scale-specific coherence, spans the λ_x axis from $y/\tan(\theta)$ to $c\delta$, following Baars and Marusic (2020) and the steps highlighted in Fig. 2(a, b). Similarly, [the premultiplied pressure spectrum due to y'-sized eddies] spans the λ_x axis from a λ_x viscous cutoff to $y/\tan(\theta)$, as sketched in Fig. 2(c). In the y-axis, the premultiplied velocity and pressure spectra span the wall-normal distance from a viscous cutoff to y'. The y viscous cut-off is at $y^+_{\text{viscous cutoff},u} \approx 100$ (Perry and Chong, 1982; Nickels et al., 2005; Hu et al., 2020). The λ_x viscous cutoff of the pressure is approximately at

$$\lambda_{x,\ \text{viscous cutoff},\ p} \sim \eta(y) = (\nu^3/\epsilon)^{1/4} \sim y^{1/4}, \tag{17}$$

following from Eq. (13). In the above equation, $\lambda_{x,\,\text{viscous cutoff},\,p}$ is the Kolmogorov length. A more often used viscous cutoff is the local Taylor

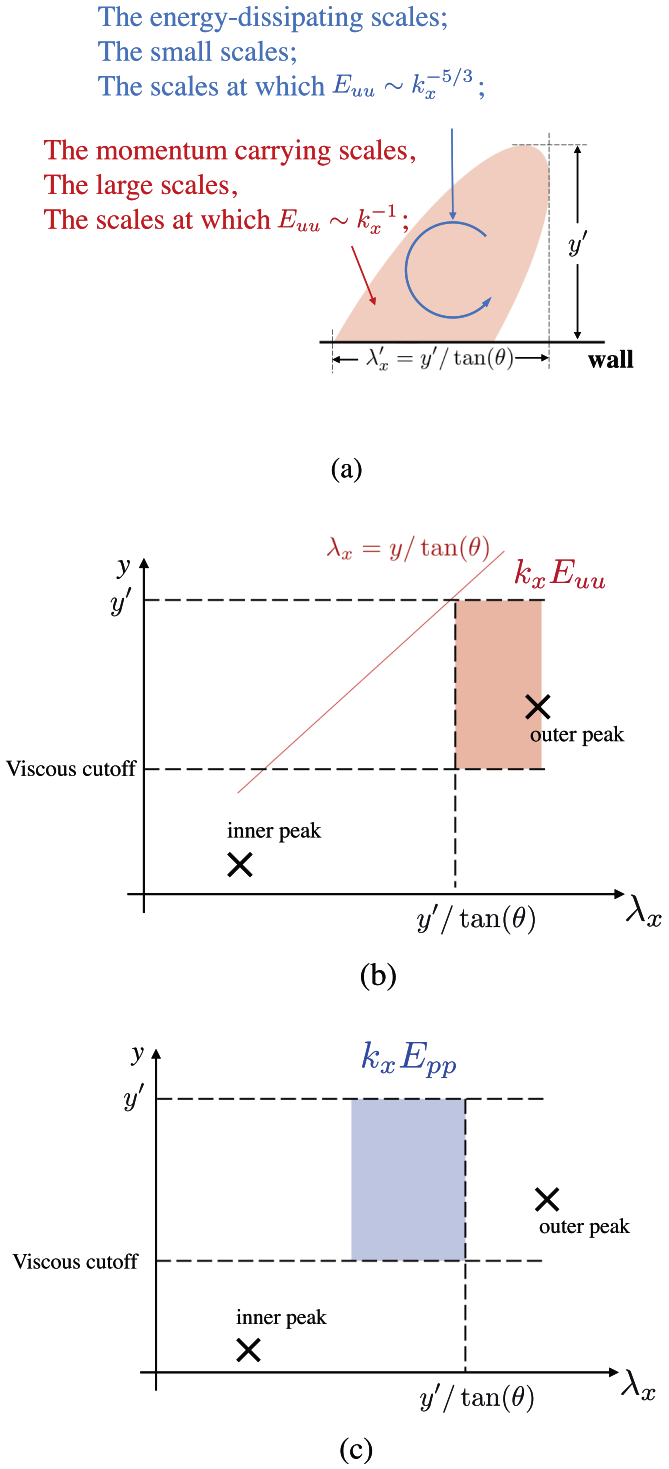

Fig. 2. (a) A sketch of y'-sized wall-attached eddies. (b, c) A sketch of the premultiplied velocity and pressure energy spectra due to y'-sized wall-attached eddies. The two axes are in logarithmic scale.

micro length

$$\lambda_{x,\ \text{viscous cutoff},\ p} \sim \lambda(y) \sim \eta(y) Re_y^{1/4} \sim y^{1/2}, \tag{18}$$

where $Re_y = yu_\tau/\nu$ is the local Reynolds number. Note that from both Eqs. (17) and (18), the λ_x viscous cutoff is an increasing function of y, which is all we need to proceed.

Formally, if one invokes Eq. (7), then

$$\begin{aligned} &[\text{premultiplied pressure spectrum due to } y'\text{-sized attached eddies}] \\ &\sim \lambda_x^{n-1} \times [\text{Dissipation due to a } y'\text{-sized eddy}]^{(3+n)/4} \\ &\sim \lambda_x^{n-1} y'^{-(3+n)/4}, \end{aligned} \tag{19}$$

where [Dissipation due to a y'-sized eddy]$\sim u_\tau^3/y$ follows from Eq. (12).

Second, we add up [pressure and velocity spectrum due to y'-sized attached eddies] for all y'. Fig. 3 sketches the basic steps. Eq. (10) still applies. Eqs. (9), (10), and (19) lead to

$$\begin{aligned} k_x E_{pp} &= \int_y^\delta [\text{premultiplied pressure spectrum due to } y'\text{-sized attached eddies}] \times \tfrac{1}{y'} dy', \\ &\sim \int_y^\delta \lambda_x^{n-1} y'^{-(7+n)/4} dy' \sim \lambda_x^{n-1} y^{-(3+n)/4}. \end{aligned} \tag{20}$$

Eq. (20) is valid for $\lambda_x < y/\tan(\theta)$. For $\lambda_x > y/\tan(\theta)$, it follows from Fig. 3 that $k_x E_{pp}$ is not a function of y and that

$$k_x E_{pp}|_{\lambda_x,\ y} = k_x E_{pp}|_{\lambda_x,\ y=\lambda_x \tan(\theta)}. \tag{21}$$

By imposing continuity at $y = \lambda_x \tan(\theta)$, Eqs. (20) and (21) together imply that

$$k_x E_{pp}|_{\lambda_x, y} \sim \lambda_x^{n-1} \lambda_x^{-(3+n)/4} \sim \lambda_x^{(3n-7)/4}. \tag{22}$$

In conclusion, re-writing Eq. (20) leads to

$$y^{-(3n-7)/4} [k_x E_{pp}] \sim (\lambda_x/y)^{n-1}, \tag{23}$$

for $\lambda_x/y < 1/\tan(\theta)$, and re-writing Eq. (22) leads to

$$y^{-(3n-7)/4} [k_x E_{pp}] \sim (\lambda_x/y)^{(3n-7)/4}, \tag{24}$$

for $\lambda_x/y > 1/\tan(\theta)$. Eqs. (23) and (24) are our main conclusions. Observe that the long anticipated scaling of $E_{pp} \sim k_x^{-1}$ in the logarithmic range, which corresponds to $\lambda_x/y > 1/\tan(\theta)$, is only valid when $n = 7/3$, which is only true at very high Reynolds numbers. Also, because Eq. (24) is a direct consequence of K41, it is also valid in the wake layer, as we will show in the next section.

4. Comparison with data

4.1. Pressure spectra

We compare Eqs. (23) and (24) to DNS data from a $Re_\tau = 5200$ channel (Lee and Moser, 2015). Fig. 4(a, b) show the re-scaled premultiplied pressure spectrum $y^{-(3n-7)/4}[k_x E_{pp}]$ as a function of λ_x/y. Data from $y^+ = 130$ to $y/\delta = 0.4$ are shown, and the logarithmic layer extends from $y^+ \approx 300$ Samie et al. (2018) to $y/\delta = 0.2$. The data in Fig. 4 include the logarithmic layer, and a wall-normal location at $y^+ = 130$, which is in the viscous layer, and a wall-normal location at $y/\delta = 0.4$, which is in the wake layer. The minimum and maximum values of λ_x present in the data are determined by the grid resolution ($\Delta_x \approx 10$) and the domain length ($L_x = 8\pi\delta$), respectively. The exponent n depends on the Reynolds number (Tsuji et al., 2007). The best fit of the present channel flow data at $Re_\tau = 5200$ yields $n = 1.9$ (up to two significant digits), which is consistent with previous measurements (Tsuji and Ishihara, 2003).

In Fig. 4(a, b), we see that the data follow Eqs. (23) and (24). Eq. (23) is valid in the inertial range with the large scale cut off at $\lambda_x \approx y/\tan(\theta)$. This range is larger away from the wall, leading to better agreement with the data in the wake layer. On the other hand, Eq. (24) is valid between $\lambda_x \approx y/\tan(\theta)$ to $\lambda_x \approx c\delta$, which range is larger closer to the wall (while still in the logarithmic layer). Fig. 5(a, b) show the compensated plots. In Fig. 5(a, b), we find plateaus at all wall-normal locations in the logarithmic layer, except for $y^+ = 130$ and $y/\delta = 0.4$, which are outside of the logarithmic layer.

Next, we compare the sketch in Fig. 3(d) to data. It directly follows from Eq. (23) that for $\lambda_x/y < 1/\tan(\theta)$, the contour lines scale as

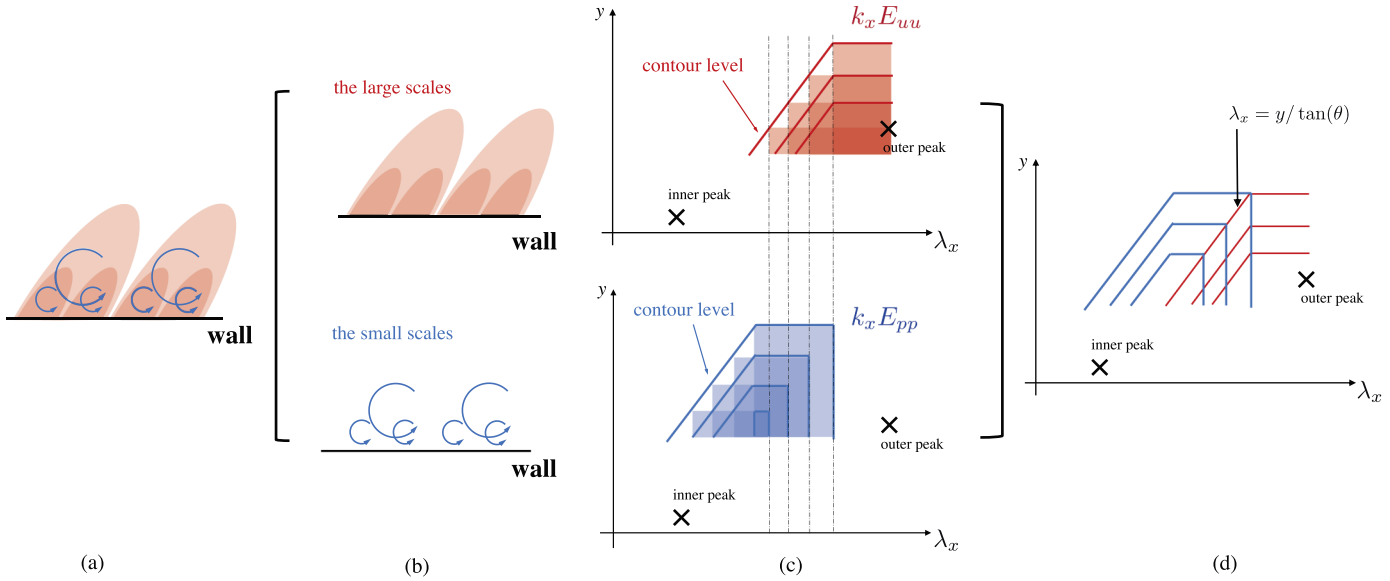

Fig. 3. (a) A sketch of the boundary layer. An eddy has both large scales and small scales. (b, c) The large scales, i.e., $y/\tan(\theta) < \lambda_x < c\delta$, contribute to the premultiplied velocity spectrum. The small scales, i.e., $\lambda_x < y/\tan(\theta)$ contribute to the premultiplied pressure spectrum. (d) Contour lines of the premultiplied velocity and pressure spectra.

$$\lambda_x^{n-1} y^{-(3+n)/4} = \text{Const}, \tag{25}$$

i.e.,

$$\log(y) \sim \frac{n-1}{(3+n)/4} \log(x) \tag{26}$$

The model proposes that: first, the peak of $k_x E_{pp}$ is located at $\lambda_x < y/\tan(\theta)$; second, the pressure spectrum decays for $\lambda_x > y/\tan(\theta)$; and third, the contour lines scale as Eq. (26). Fig. 6 shows the premultiplied velocity and pressure spectra in a $Re_\tau = 5200$ channel. The data is from $y^+ = 300$ (i.e., $y^+ \approx 4\sqrt{5200}$) to $y/\delta = 1$ (i.e., $y^+ = 5200$). Comparing Figs. 6 and 3 (d), the model works qualitatively well. From a quantitative standpoint: first, the peak of $k_x E_{pp}$ is located at a scale to the left of $y/\tan(\theta)$, and second, $k_x E_{pp}$ decays for $\lambda_x > y/\tan(\theta)$. This validates the model and shows unambiguously that pressure fluctuations are most energetic at small scales. Lastly, for $\lambda_x < y/\tan(\theta)$, the scalings of the pressure contour lines follow Eq. (26) closely.

4.2. Finite Reynolds number and the −7/3 scaling

The scaling exponent n depends on the Reynolds number. Fig. 7(a) shows the scaling n as a function of the Taylor micro length scale Reynolds number Re_λ in isotropic homogeneous turbulence. Details of the data can be found in Tsuji and Ishihara (2003) and the references cited therein. The scaling n is about 1.9 at $Re_\lambda = 200$, and is 7/3 for $Re_\lambda > 600$. To make use of Fig. 7(a), we compute the Taylor micro length scale Reynolds number Re_λ of a λ_x-sized eddy. First, the Reynolds number of a λ_x-sized eddy is

$$Re \approx \frac{U_c \lambda_x}{\nu}, \tag{27}$$

where U_c is the characteristic velocity length scale

$$U_c = (\epsilon\lambda_x)^{1/3} = \left(\frac{u_\tau^3}{\kappa y}\lambda_x\right)^{1/3} = \left(\frac{u_\tau^3}{\kappa \tan(\theta)}\right)^{1/3} \approx 2.4u_\tau. \tag{28}$$

Here, a λ_x-sized eddy is an eddy of height $y = \lambda_x \tan(\theta)$; and at $y = \lambda_x \tan(\theta)$, the dissipation equals the production and is $u_\tau^3/\kappa y$. Plugging Eq. (28) into Eq. (27), the local Reynolds number is

$$Re = 2.4u_\tau \lambda_x/\nu = 13.6y^+ \tag{29}$$

which translate to a Taylor micro length scale Reynolds number

$$Re_\lambda = \sqrt{10Re} \approx 11.7\sqrt{y^+}. \tag{30}$$

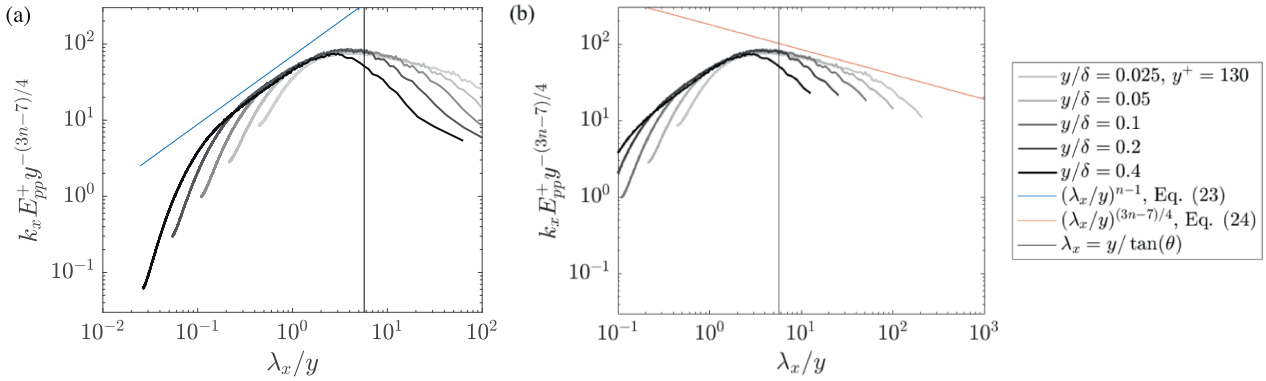

Fig. 4. (a) Re-scaled and premultiplied pressure spectrum $y^{-(3n-7)/4}[k_x E_{pp}]$ as a function of λ_x/y at $y/\delta = 0.025$, 0.05, 0.1, 0.2, and 0.4 in a $Re_\tau = 5200$ channel. The thin blue solid line shows the slope $n-1$. The thin black solid line is at $\lambda_x/\tan(\theta)$. (b) Re-scaled and premultiplied pressure spectrum $y^{-(3n-7)/4}[k_x E_{pp}]$ as a function of λ_x/y at $y/\delta = 0.025$, 0.05, 0.1, 0.2, and 0.4 in a $Re_\tau = 5200$ channel. The thin red solid line shows the slope of $(3n-7)$. (For interpretation of the references to colour in this figure legend, the reader is referred to the web version of this article.)

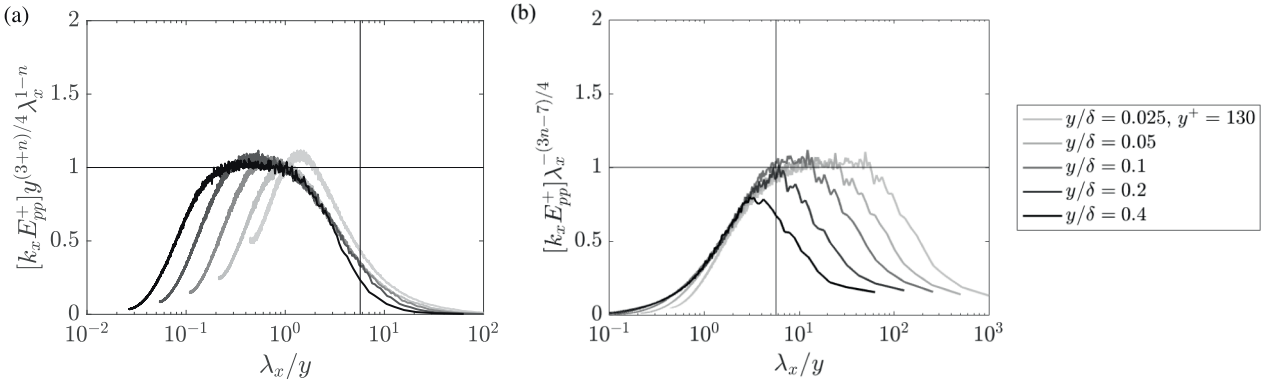

Fig. 5. (a) Compensated plot of Fig. 4(a). (b) Compensated plot of Fig. 4(b).

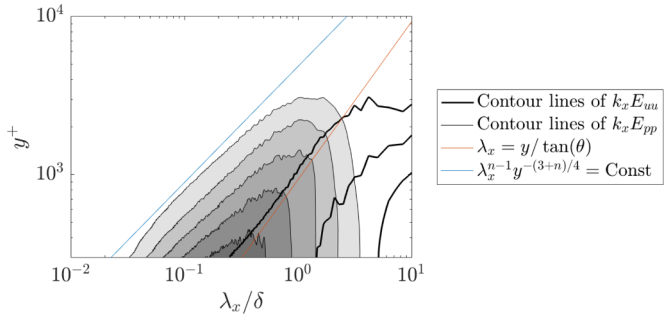

Fig. 6. Contours of the premultiplied velocity spectrum (black bold solid lines) and the premultiplied pressure spectrum (color contours, darker colors denote larger contour values). The thin blue line corresponds to Eq. (25). The thin red line corresponds to $\lambda_x = y/\tan(\theta)$, and the scaling indicated by the thin blue line should only be observed to the left of the thin red line. (For interpretation of the references to colour in this figure legend, the reader is referred to the web version of this article.)

The logarithmic layer is approximately from $y^+ = 4\sqrt{Re_\tau}$ to $y/\delta = 0.2$. At $y^+ = 4\sqrt{Re_\tau}$, $Re_\lambda = 23.4 Re_\tau^{1/4}$, and at $y/\delta = 0.2$, $Re_\lambda = 5.23 Re_\tau^{1/2}$. Fig. 7 shows the Taylor micro length scale Reynolds number Re_λ at $y^+ = 4\sqrt{Re_\tau}$ and at $y/\delta = 0.2$ as a function of the friction Reynolds number Re_τ. For a $Re_\tau = 5200$ channel, Re_λ is $O(200 - 300)$ in the logarithmic layer, and it follows from Fig. 7(a) that $n \approx 1.9$. According to Fig. 7(b), we expect the pressure spectrum in the logarithmic layer follows the -7/3 scaling at $Re_\tau > 4.3 \times 10^5$. In Appendix A, we will further discuss the Reynolds number effects.

5. Hierarchical random additive process

In Section 3.2.1, we concluded that [pressure variance of a y'-sized attached eddy]$\sim u_\tau^4$ is not a function of y'. This suggests that pressure fluctuations due to attached eddies are self-similar, which in turn suggests that we could model pressure fluctuations in a wall-bounded flow as a hierarchical random additive process (HRAP) following Yang et al. (2016), and Yang and Abkar (2018). Doing this will leads to additional scaling predictions, which can be compared with data to further validate our model.

The HRAP model for pressure reads

$$p' = \sum_{i=1}^{N_y} b_i, \quad N_y \sim \log(\delta/y), \tag{31}$$

where the addend b_i is pressure fluctuation due to a y_i-sized eddy, and b_i are statistically identical and independent variables. The number of addend depends on the wall-normal distance. For instance, at $y = \delta$, only one hierarchy of attached eddies contribute, and therefore $N_y = 1$ at $y = \delta$; at $y = \delta/2$, two hierarchies of attached eddies contribute, and

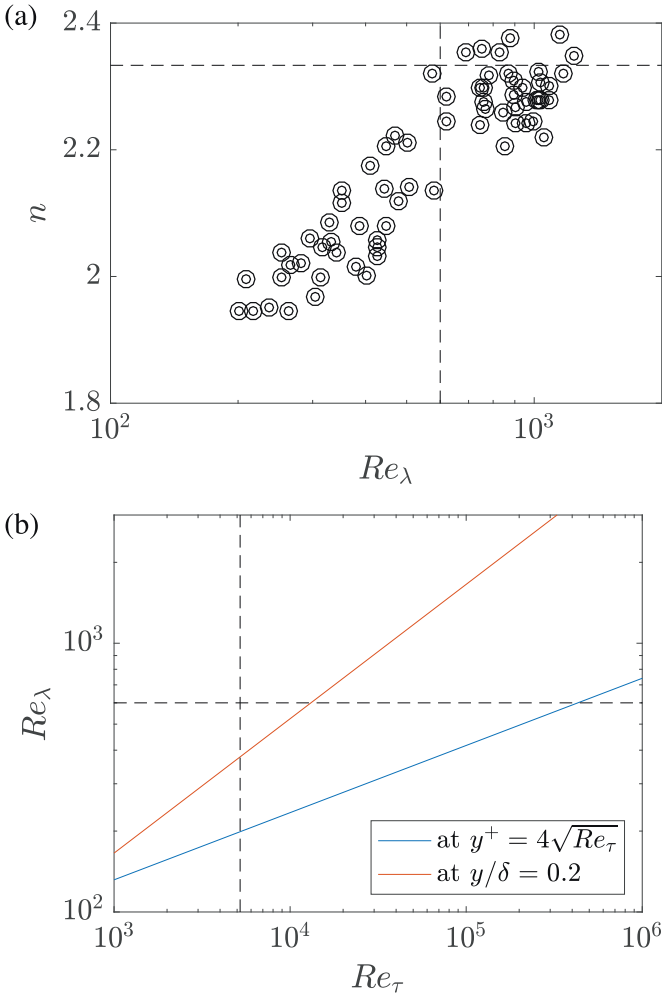

Fig. 7. (a) The scaling exponent of the pressure spectrum n in isotropic homogeneous turbulence as a function of the Taylor micro length scale Reynolds number Re_λ. Details of the measurements can be found in Tsuji and Ishihara (2003) and the references cited therein. The two dashed lines are at $n = 7/3$ and $Re_\lambda = 600$. (b) The Taylor micro length scale Reynolds number as a function of the friction Reynolds number at $y^+ = 4\sqrt{Re_\tau}$ and $y/\delta = 0.2$. The two dashed lines are at $Re_\tau = 5200$, and $Re_\lambda = 600$.

therefore $N_y = 2$ at $y = \delta/2$; at $y = \delta/4$, three hierarchies of attached eddies contribute, and therefore $N_y = 3$ at $y = \delta/4$. Generally, at $y = \delta/2^{n+1}$, n hierarchies of attached eddies contribute, and $N_y = n$ at $y = \delta/2^{n+1}$, or, $N_y \sim \log(\delta/y)$. Eq. (31) is essentially Eq. (10), but compared to Eq. (10), using Eq. (31) to compute pressure statistics is

much more straight-forward. For example, squaring both sides of Eq. (31) and averaging, we get

$$\langle p'p' \rangle = \sum_{i=1}^{N_y} \langle b_i^2 \rangle \sim N_y \langle b^2 \rangle \sim \log(\delta/y) \tag{32}$$

which is Eq. (1).

In the following, we make use of Eq. (31) and study the statistical behavior of pressure in wall-bounded flows. Per Eq. (32), $p'p'$ is a sum of b_i^2, which are identically independent distributed random variables. Following Meneveau and Marusic (2013) and invoking the central limit theorem, we get

$$\langle p'^{2m} \rangle^{1/m} = A_{m,p} \log(\delta/y) + B_{m,p}, \tag{33}$$

where $A_{m,p} = [(2m-1)!!]^{1/m} A_{1,p}$. The above derivation has not been presented before, but the presence of the logarithmic scalings in Eq. (33) was previously observed by Mehrez et al. (2019), where conditional sampling of the flow fields shows that positive pressure fluctuations locate between the legs of hairpin eddies and negative pressure fluctuations near the heads of the hairpin eddies within vortical cores. Next, we compute the pressure moment generating functions (MGFs), i.e., $< \exp(qp') >$. From Eq. (31), we have

$$\begin{aligned} \langle \exp(qp') \rangle &= \langle \textstyle\prod_{i=1}^{N_y} \exp(qb_i) \rangle \\ &= \langle \exp(qb) \rangle^{N_y} \sim (\delta/y)^{\log \langle \exp(qb) \rangle}. \end{aligned} \tag{34}$$

leading to a power-law, where q is a "dialing" parameter, and we have used the identity $\alpha^{\ln\beta} = \beta^{\ln\alpha}$ for the last " $\sim$ ". If b is Gaussian, then

$$\tau(q) \equiv \log \langle \exp(qb) \rangle = Cq^2. \tag{35}$$

From the MGFs, one can compute the variance of the pressure fluctuations

$$\langle p'^m \rangle = \left. \frac{d^n \langle \exp(qp') \rangle}{dq^m} \right|_{q=0}. \tag{36}$$

Plugging Eqs. (34) and (35) in Eq. (36), we have

$$\langle p'p' \rangle = 2C \log(\delta/y) + \text{ Const}, \tag{37}$$

and therefore $A_{1,p} = 2C$. Eq. (34) is a "strong" scaling and is valid only in the logarithmic layer. The following is a weak form of the scaling in Eq. (34)

$$\langle \exp(qp') \rangle \sim \langle \exp(q_o p') \rangle^{\Phi(q,q_o)}, \tag{38}$$

where q_o is a constant, Φ is the exponent. This weak form is known as the extended self-similarity (ESS) (De Silva et al., 2017; Krug et al., 2017). While Eq. (34) is only possible if the addends in Eq. (31) are identically independently distributed, $< \exp(qp') >$ is a power law of $< \exp(q_o p') >$ as long as the addends are independent. This property is particularly useful at finite Reynolds numbers, where the extent of the log layer is limited. The above scalings in Eqs. (33), (34), and (38) are consequences of our model. In the following, we will test our model by comparing these scalings to data.

6. Further comparison with data

In this section, we compare the scalings to the $Re_\tau = 5200$ channel flow DNS (Lee and Moser, 2015). Fig. 8 shows $< p'^{2m} >^{1/m}$ as a function of the wall-normal distance for $m = 1$, 2, 3, and 4. The data shows wiggles for $m = 3$ and 4. Nonetheless, the logarithmic scaling in Eq. (33) can be found in the logarithmic layer, i.e., from $y^+ = 4\sqrt{Re_\tau}$ to $y/\delta = 0.2$, and even beyond the logarithmic layer, i.e., from $y^+ = 150$ to $y/\delta = 0.4$, for m=1, 2, 3, and 4. Fitting the data in the logarithmic layer to Eq. (33) yields $A_{1,p} = 2.5$, $A_{2,p}/A_{1,p} = 2.6$, $A_{3,p}/A_{1,p} = 6.2$, and $A_{3,p}/A_{1,p} = 12.8$. The numerical value of $A_{1,p}$ is very close to that of $A_{1,u}$. This may just be a coincidence. To the best of our knowledge, there has not been a theory that directly relates pressure variance and velocity variance. The data shows super-Gaussian behaviors, i.e., $A_{2,p}/A_{1,p} > \sqrt{3}$, $A_{3,p}/A_{1,p} > (3 \times 5)^{1/3}$, and $A_{3,p}/A_{1,p} > (3 \times 5 \times 7)^{1/4}$. This suggests that pressure fluctuations are more intermittent than streamwise velocity fluctuations, which are sub-Gaussian (Meneveau and Marusic, 2013).

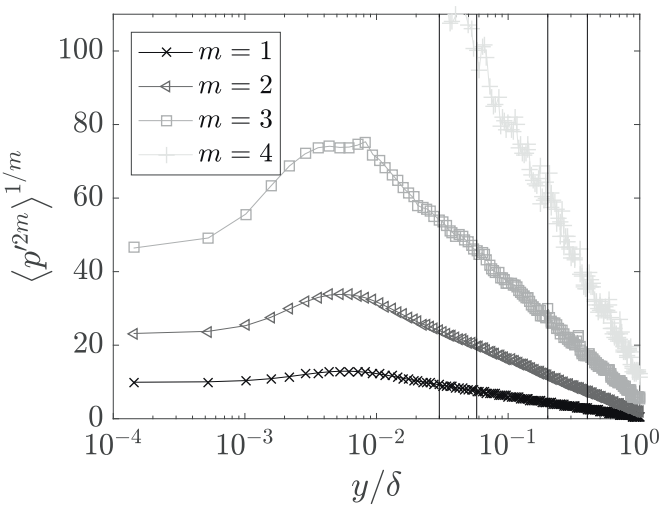

Fig. 8. (a) $< p'^{2m} >^{1/m}$ as a function of the wall-normal distance for $m = 1$, 2, 3, and 4. The thin solid lines are at $y^+ = 150$, $4\sqrt{Re_\tau}$, and $y/\delta = 0.2$, 0.4. Fitting the data to Eq. (33) yields $A_{1,p} = 2.5$, $A_{2,p} = 6.6$, $A_{3,p} = 15.5$, and $A_{4,p} = 32.3$. The pressure data are normalized by the friction velocity.

Fig. 9 (a) shows the pressure probability density function (PDF). The pressure fluctuations are negatively skewed, i.e., it is more likely to encounter a large negative pressure fluctuation than a large positive pressure fluctuation. This makes negative pressure fluctuations statistically more important than positive pressure fluctuations in determining high-order statistics. Fig. 9(b, c) show the premultiplied pressure PDFs, i.e., $p^2 \times PDF$ and $p^4 \times PDF$. If one knows the PDF of, e.g., a random variable ϕ, $< f(\phi) >$ could be computed from $\int$ [PDF of ϕ]$f(\phi')d\phi'$, where the integrand is the premultiplied PDF. Thus, premultiplied PDFs are useful tools when studying the statistical convergence of statistical objectives. Here, from Fig. 9(b, c), we see that positive pressure fluctuations lead to a higher peak than the negative pressure fluctuations in the low order statistics $< p'p' >$ and negative pressure fluctuations lead to a higher peak than the positive pressure fluctuations in the high order statistics $< p'^4 >$. Comparing the PDFs at $y^+ = 300$ (i.e., $y^+ = 4\sqrt{4Re_\tau}$) and $y/\delta = 0.2$, we see from Fig. 9(a) that it is more likely to encounter large fluctuations near the wall than away from the wall in the logarithmic layer. This makes large fluctuations statistically more significant near the wall than away from the wall. Lastly, from Fig. 9(b, c), we could also conclude that the data is statistically converged for $m = 1$ and 2.

Fig. 10 (a) shows the MGFs $< \exp(qp') >$ as a function of the wall-normal distance for $q = 0.2$, 0.3, and 0.4. The power law scaling in Eq. (34) could be found in the logarithmic layer and slightly beyond the logarithmic layer, i.e., from $y^+ = 150$ to $y/\delta = 0.4$ for $q = 0.2$, 0.3, and 0.4. Fig. 10(b, c) shows the premultiplied pressure PDFs, i.e., $\exp(0.1p') \times$ PDF and $\exp(0.1p') \times$ PDF. Again, we conclude from Fig. 10(b, c) the data is converged for both $q = 0.1$ and 0.4. The MGF $< \exp(qp') >$ emphasizes large pressure fluctuations that have the same sign as q. This is particularly the case for large valued $|q|$. Comparing Fig. 10(b, c), we see that the positive pressure fluctuations play a more important role for $< \exp(0.4p') >$ than for $< \exp(0.1p') >$. Comparing the premultiplied PDFs at $y^+ = 300$ and $y/\delta = 0.2$, we could also see that the large fluctuations are statistically more important near the wall than away from the wall.

Fig. 11 shows the power-law exponents as a function of q obtained by fitting the data in Fig. 10(a) to Eq. (34). In the beginning of the

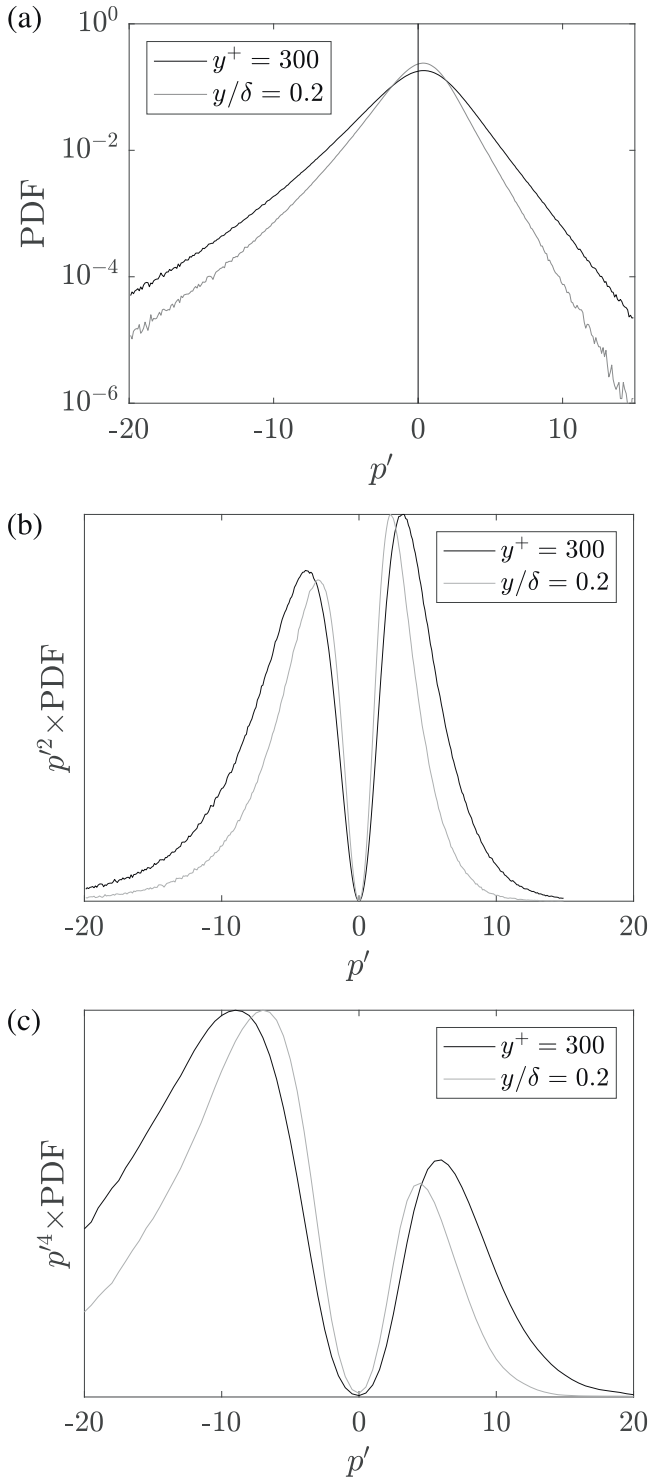

Fig. 9. (a) Pressure probability density function (PDF). (b, c) Premultiplied pressure PDF. The data are normalized.

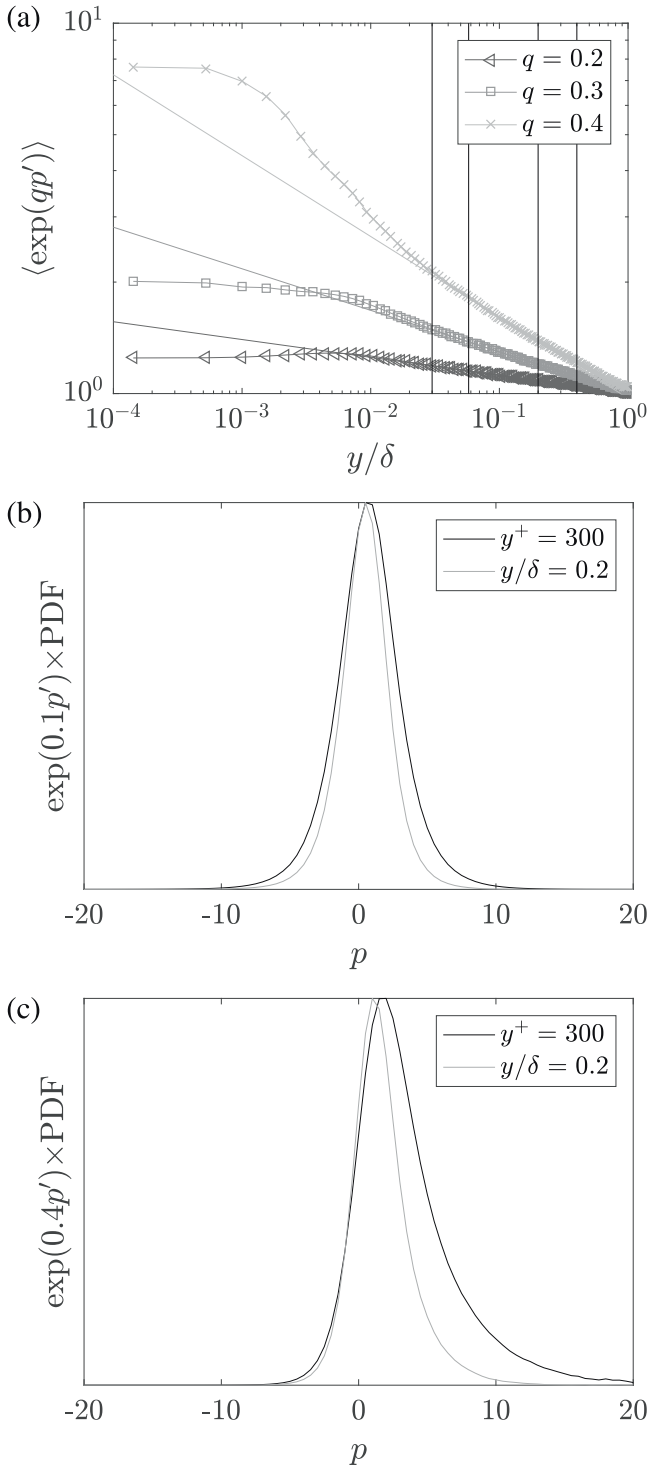

Fig. 10. (a) MGFs $< \exp(qp') >$ as a function of the wall-normal distance for $q = 0.2$, 0.3 and 0.4. The solid lines at constant y locations are $y^+ = 150$, $4\sqrt{Re_\tau}$, and $y/\delta = 0.2$, 0.4. Fits of the data to Eq. (34) are also shown for reference. The slopes of the fits are shown in Fig. 11 and are not repeated here for brevity. (b, c) Premultiplied pressure PDFs.

section, we conclude that if the addends in Eq. (31) are Gaussian, the power-law exponent is quadratic. According to Fig. 11, Gaussianality provides a good approximation for $\tau(q)$ near $q = 0$. Considering that the small-valued $|p'|$ dominate $< \exp(qp') >$ for q near 0, the fact that $\tau(q) \sim q^2$ near $q = 0$ suggests that the small valued pressure fluctuations are approximately Gaussian. Fitting $\tau(q)$ near $q = 0$ yields $\tau_q = 1.3 \cdot q^2$. Earlier in this section, we conclude that $A_{1,p} = 2C$. This bears out in data since $A_{1,p} = 2.6$ and $C = 1.3$. For q values away from $q = 0$, we see that the data follows $\tau(q) = 1.3q^2$ well on the positive side but not on the negative side. Considering that $< \exp(qp') >$ emphasizes pressure fluctuations that have the same sign as q, this suggests that negative pressure fluctuations are less Gaussian than positive pressure fluctuations, which is consistent with Fig. 9(a).

Last, Fig. 12 shows $< \exp(qp') >$ as a function of $< \exp(q_0 p') >$

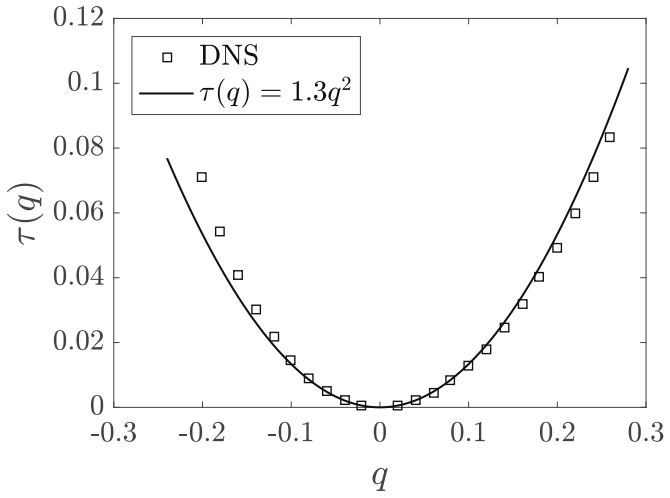

Fig. 11. Power-law exponent of the MGFs as a function of q. $\tau(q) = 1.3q^2$ is the best fit of the data near $q = 0$.

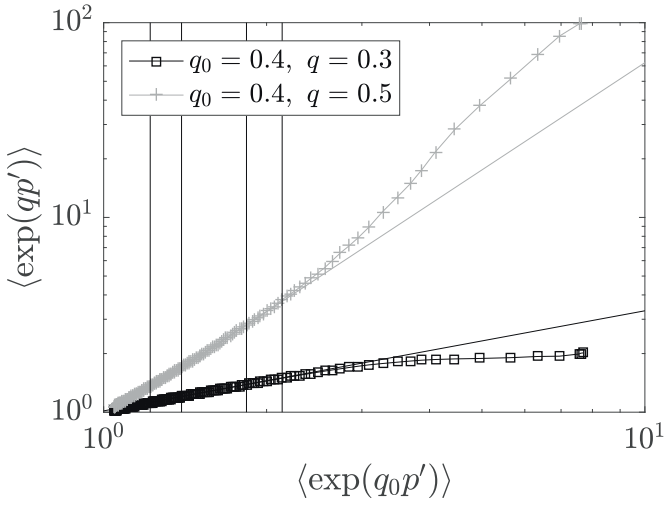

Fig. 12. ESS scalings for $q_0 = 0.4$, and $q = 0.3$, 0.5. The vertical lines are at constant $< \exp(q_0 p') >$ values 1.2, 1.4, 1.8 and 2.1, respectively.

for $q_0 = 0.4$ and $q = 0.3$, 0.5. The power law scaling in Eq. (38) are found in the logarithmic layer, which corresponds to $1.4 < < \exp(q_0 p') > < 1.8$, and slightly beyond the logarithmic layer from $y^+ = 150$ to $y/\delta = 0.4$, which corresponds to $1.2 < < \exp(q_0 p') > < 2.1$. (Note that $< \exp(q_0 p') >$ is a decreasing function of the wall-normal distance.)

7. Conclusion

In this work, we invoke Kolmogorov's theory of small-scale turbulence and Townsend's attached eddy hypothesis to model pressure fluctuations in high Reynolds number wall-bounded flows. Our derivation that acknowledges the fact that pressure is a small-scale quantity and is also consistent with the attached eddy hypothesis. Specifically, our model relies on Eq. (7), a direct consequence of K41, and Eq. (10), a direct consequence of AEH, and no additional modeling assumptions are introduced. The model yields

$$y^{-(3n-7)/4}[k_x E_{pp}] \sim (\lambda_x/y)^{n-1} \quad \text{for} \quad \lambda_x/y < 1/\tan(\theta).$$

and

$$y^{-(3n-7)/4}[k_x E_{pp}] \sim (\lambda_x/y)^{(3n-7)/4} \quad \text{for} \quad \lambda_x/y > 1/\tan(\theta),$$

where $\theta \approx 10^\circ$ is the attached eddy inclination angle, the Reynolds number dependent power-law exponent n takes the value 7/3 at high Reynolds numbers ($Re_\tau = O(10^5)$) and 1.9 in $Re_\tau = 5200$ channel. The data collapse without explicitly accounting for shear and flow anisotropy as a function of the wall-normal distance. In addition, we extend the model to a hierarchical random additive one, i.e.,

$$p' = \sum_{i=1}^{N_y} b_i, \quad N_y \sim \log(\delta/y),$$

where b_i's are identically, independently, distributed random addends. The above formulation admits logarithmic scalings of even order central moments as well as the power-law scalings of the moment generating functions, both of which are found in data.

CRediT authorship contribution statement

Haosen H.A. Xu: Conceptualization, Formal analysis, Investigation. **Aaron Towne:** Writing - review & editing. **Xiang I.A. Yang:** Writing - review & editing. **Ivan Marusic:** Writing - review & editing.

Declaration of Competing Interest

The authors are not aware of any conflict of interest.

Acknowledgements

XY would like to thank A. Lozano-Duran and J. Jimenez for fruitful discussion. XY would also like to thank W. Wu and C. Meneveau for their help in accessing the channel flow data at the Johns Hopkins Turbulence Database. M.-K. Lee and A. Lozano-Duran are gratefully acknowledge for their generosity in sharing the DNS data. Financial support from Office of Naval Research (award number N00014-20-1-2315) is gratefully acknowledged.

Appendix A. Viscous cutoff and finite Reynolds number effects

The discussion in Section 3 is only valid at scales where neither the flow geometry (scale δ) nor the viscosity (scale ν/u_τ or $(\nu^3/\epsilon)^{1/4}$) has an effect. In the wall-normal direction, this limits the discussion in Section 3 to the logarithmic layer, i.e., away from the "inner peak". Fig. A.13(a) shows the premultiplied streamwise velocity spectrum of channel flow at $Re_\tau = 1000$, 2000, and 5200. The inner peak (marked by a $\times$ symbol) is located at $\lambda^+_{x,\text{innerpeak}} \approx 800$, $y^+ = 13$. Following Baars and Marusic (2018), $y^+ \approx 100$ is sufficiently away from the inner peak, above which viscous effects are negligible. Plot two lines at $\lambda^+_{x,\text{innerpeak}} \approx 800$ and at $y^+ \approx 100$. The premultiplied velocity spectrum at $\lambda^+_{x,\text{innerpeak}} \approx 800$ and $y^+ \approx 100$ is 0.36 of the inner peak value. If we follow the above discussion and define the wall-normal height at which the premultiplied spectrum is 0.36 of its peak value to be the height above which the viscous effects are negligible, we can find the heights at which Townsend's attached eddy hypothesis works for $k_x E_{pp}$ and $k_x E_{ww}$. Fig. A.13(b, c) shows the premultiplied pressure and spanwise velocity spectra. The inner peaks of the premultiplied pressure and spanwise velocity spectra locate at the streamwise wavelengths $\lambda^+_{x,\text{innerpeak}} = 272$ and 306, and the wall-normal heights $y^+ = 23$ and 39, respectively. The premultiplied pressure and spanwise velocity spectra is 0.36 of their peak values at $y^+ = 210$ and 615, above which viscous effects are negligible. Requiring one decade of scales from the viscous cutoff to $y = 0.4\delta$ in $k_x E_{uu}$, $k_x E_{pp}$, and $k_x E_{ww}$, the Reynolds number must be greater than $Re_\tau \approx 2500$, $Re_\tau \approx 5000$, and $Re_\tau \approx 15000$, respectively. Hence, to be able to explain the statistical behaviors of the spanwise velocity fluctuations in the framework of Townsend's attached eddy hypothesis, one needs to be at a Reynolds number $Re_\tau \gg 5200$.

To make this point clearer, we look at Fig. A.14, where we show the premultiplied spanwise velocity spectra in a $Re_\tau = 5200$ channel and a

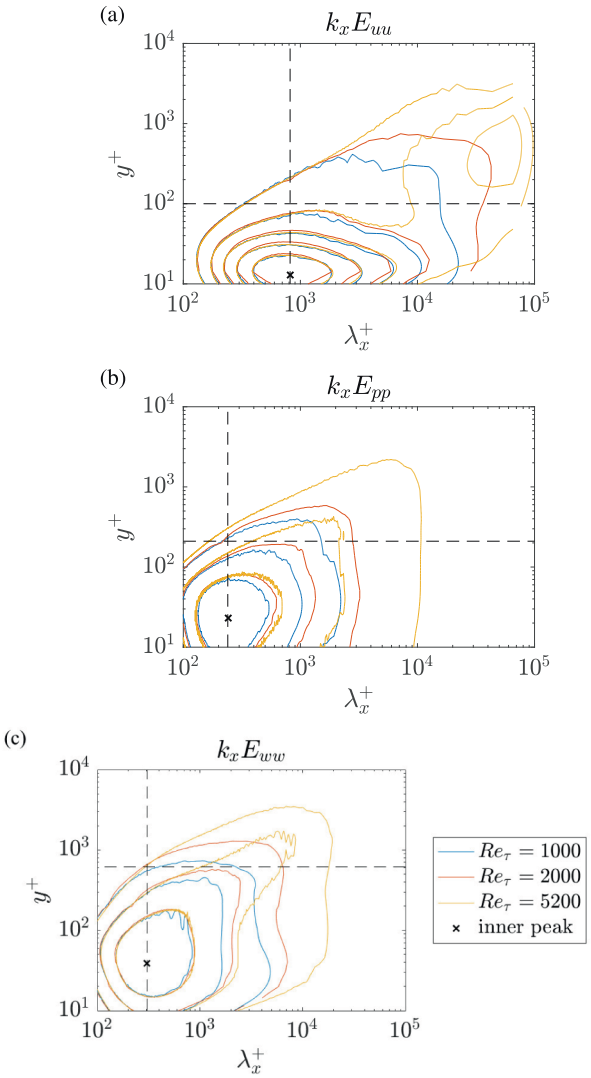

Fig. A13. (a) Premultiplied streamwise velocity spectra in channel flow at $Re_\tau = 1000$ (Graham et al., 2016), $Re_\tau = 2000$ (Hoyas and Jiménez, 2006), and $Re_\tau = 5200$ (Lee and Moser, 2015). The two dashed lines are at $y^+ = 100$ and $\lambda_x^+ = 816$, respectively. The cross symbol indicates the inner peak. (b) Premultiplied pressure spectra in channel flow at $Re_\tau = 1000$, $Re_\tau = 2000$, and $Re_\tau = 5200$. The two dashed lines are at $y^+ = 210$ and $\lambda_x^+ = 272$. The cross symbol indicates the inner peak. (c) Premultiplied spanwise spectra in channel flow at $Re_\tau = 1000$, $Re_\tau = 2000$, and $Re_\tau = 5200$. The two dashed lines are at $y^+ = 615$ and $\lambda_x^+ = 306$. The cross symbol indicates the inner peak.

$Re_\tau = 10000$ boundary layer (Baidya et al., 2012). The second peak in E_{ww}, which should be present at high Reynolds numbers and is present in the $Re_\tau = 10000$ boundary layer, could not be found in the $Re_\tau = 5200$ channel. Also, the contour lines, which should follow $\lambda_x \sim y$ and follow $\lambda_x \sim y$ in the $Re_\tau = 10000$ boundary layer, do not follow $\lambda_x \sim y$ in the $Re_\tau = 5200$ channel. In conclusion, at $Re_\tau = 5200$, the spanwise velocity is subjected to non-negligible finite Reynolds number effect, and one needs to exercise extra caution if Townsend's attached eddy is invoked to interpret the spanwise velocity data, particularly when drawing an analogy between pressure fluctuations and spanwise velocity fluctuations (Jimenez and Hoyas, 2008).

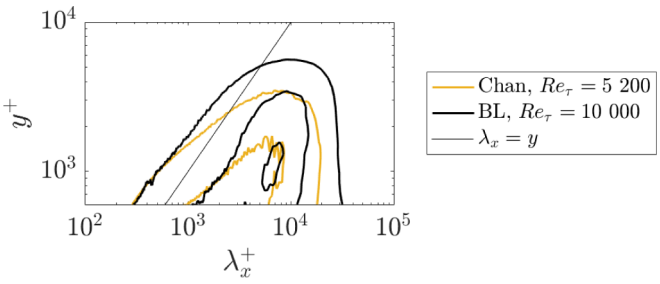

Fig. A14. Premultiplied spanwise velocity spectra in a $Re_\tau = 5200$ channel and a $Re_\tau = 10000$ boundary layer. The thin solid line shows $\lambda_x \sim y$.

Supplementary material

Supplementary material associated with this article can be found, in the online version, at 10.1016/j.ijheatfluidflow.2020.108620

References

Abe, H., Matsuo, Y., Kawamura, H., 2005. A DNS study of Reynolds-number dependence on pressure fluctuations in a turbulent channel flow. TSFP DIGITAL LIBRARY ONLINE. Begel House Inc.

Albertson, J.D., Katul, G.G., Parlange, M.B., Eichinger, W.E., 1998. Spectral scaling of static pressure fluctuations in the atmospheric surface layer: the interaction between large and small scales. Phys. Fluids 10 (7), 1725–1732.

Baars, W. J., Marusic, I., 2018. Data-driven decomposition of the streamwise turbulence kinetic energy in boundary layers. Part 1: energy spectra. arXiv:1810.03100.

Baars, W.J., Marusic, I., 2020. Data-driven decomposition of the streamwise turbulence kinetic energy in boundary layers. Part 1. Energy spectra. J. Fluid Mech. 882.

Baidya, R., Philip, J., Hutchins, N., Monty, J., Marusic, I., 2012. Measurements of streamwise and spanwise fluctuating velocity components in a high Reynolds number turbulent boundary layer. Measurements 3, 7.

Bradshaw, P., 1967. “Inactive” motion and pressure fluctuations in turbulent boundary layers. J. Fluid Mech. 30 (2), 241–258.

Cao, N., Chen, S., Doolen, G.D., 1999. Statistics and structures of pressure in isotropic turbulence. Phys. Fluids 11 (8), 2235–2250.

Christensen, K., Adrian, R.J., 2001. Statistical evidence of hairpin vortex packets in wall turbulence. J. Fluid Mech. 431, 433–443.

Corrsin, S., 1951. On the spectrum of isotropic temperature fluctuations in an isotropic turbulence. J. Appl. Phys. 22 (4), 469–473.

De Silva, C.M., Krug, D., Lohse, D., Marusic, I., 2017. Universality of the energy-containing structures in wall-bounded turbulence. J. Fluid Mech. 823, 498–510.

Elliott, J.A., 1972. Microscale pressure fluctuations measured within the lower atmospheric boundary layer. J. Fluid Mech. 53 (2), 351–384.

Gotoh, T., Fukayama, D., 2001. Pressure spectrum in homogeneous turbulence. Phys. Rev. Lett. 86 (17), 3775.

Graham, J., Kanov, K., Yang, X.I.A., Lee, M., Malaya, N., Lalescu, C.C., Burns, R., Eyink, G., Szalay, A., Moser, R.D., et al., 2016. A web services accessible database of turbulent channel flow and its use for testing a new integral wall model for LES. J. Turbul. 17 (2), 181–215.

Hoyas, S., Jiménez, J., 2006. Scaling of the velocity fluctuations in turbulent channels up to $Re_\tau = 2003$. Phys. Fluids 18 (1), 011702.

Hu, R., Yang, X.I., Zheng, X., 2020. Wall-attached and wall-detached eddies in wall-bounded turbulent flows. J. Fluid Mech. 885.

Jiménez, J., 2012. Cascades in wall-bounded turbulence. Ann. Rev. Fluid Mech. 44.

Jimenez, J., Hoyas, S., 2008. Turbulent fluctuations above the buffer layer of wall-bounded flows. J. Fluid Mech. 611, 215–236.

Kim, J., 1989. On the structure of pressure fluctuations in simulated turbulent channel flow. J. Fluid Mech. 205, 421–451.

Kim, J., Moin, P., Moser, R., 1987. Turbulence statistics in fully developed channel flow at low Reynolds number. J. Fluid Mech. 177, 133–166.

Kolmogorov, A.N., 1941. The local structure of turbulence in incompressible viscous fluid for very large Reynolds numbers. Dokl. Akad. Nauk SSSR. vol. 30. pp. 299–303.

Krug, D., Yang, X.I.A., De Silva, C.M., Ostilla-Mónico, R., Verzicco, R., Marusic, I., Lohse, D., 2017. Statistics of turbulence in the energy-containing range of Taylor–Couette compared to canonical wall-bounded flows. J. Fluid Mech. 830, 797–819.

Lauchle, G.C., Daniels, M.A., 1987. Wall-pressure fluctuations in turbulent pipe flow. Phys. Fluids 30 (10), 3019–3024.

Lee, M., Moser, R.D., 2015. Direct numerical simulation of turbulent channel flow up to $Re_\tau \approx 5200$. J. Fluid Mech. 774, 395–415.

Liu, X., Katz, J., 2006. Instantaneous pressure and material acceleration measurements using a four-exposure PIV system. Exp. Fluids. 41 (2), 227.

Marusic, I., Heuer, W.D., 2007. Reynolds number invariance of the structure inclination angle in wall turbulence. Phys. Rev. Lett. 99 (11), 114504.

Marusic, I., Monty, J.P., 2019. Attached eddy model of wall turbulence. Ann. Rev. Fluid Mech. 51, 49–74.

Marusic, I., Monty, J.P., Hultmark, M., Smits, A.J., 2013. On the logarithmic region in wall turbulence. J. Fluid Mech. 716.

Mehrez, A., Philip, J., Yamamoto, Y., Tsuji, Y., 2019. Pressure and spanwise velocity fluctuations in turbulent channel flows: logarithmic behavior of moments and coherent structures. Phys. Rev. Fluids 4 (4), 044601.

Meneveau, C., Marusic, I., 2013. Generalized logarithmic law for high-order moments in turbulent boundary layers. J. Fluid Mech. 719.

Nickels, T.B., Marusic, I., Hafez, S., Chong, M.S., 2005. Evidence of the k^{-1} law in a high-Reynolds-number turbulent boundary layer. Phys. Rev. Lett. 95 (7), 074501.

Obukhov, A., 1949. The local structure of atmospheric turbulence. Dokl. Akad. Nauk. SSSR. vol. 67. pp. 643–646.

Panton, R.L., Lee, M., Moser, R.D., 2017. Correlation of pressure fluctuations in turbulent wall layers. Phys. Rev. Fluids 2 (9), 094604.

Patwardhan, S.S., Ramesh, O.N., 2014. Scaling of pressure spectrum in turbulent boundary layers. Journal of Physics: Conference Series. vol. 506. IOP Publishing, pp. 012011.

Perry, A.E., Chong, M.S., 1982. On the mechanism of wall turbulence. J. Fluid Mech. 119, 173–217.

Pope, S.B., 2001. Turbulent flows. Cambridge: Cambridge University Press.

Samie, M., Marusic, I., Hutchins, N., Fu, M., Fan, Y., Hultmark, M., Smits, A., 2018. Fully resolved measurements of turbulent boundary layer flows up to $Re_\tau = 20,000$. J. Fluid Mech. 851, 391–415.

Smits, A.J., McKeon, B.J., Marusic, I., 2011. High-Reynolds number wall turbulence. Ann. Rev. Fluid Mech. 43.

Townsend, A., 1976. The Structure of Turbulent Shear Flow, second ed. Cambridge University Press, Cambridge.

Tsuji, Y., 2007. Lagrangian acceleration measurement in fully developed turbulence. TSFP DIGITAL LIBRARY ONLINE. Begel House Inc.

Tsuji, Y., Fransson, J.H., Alfredsson, P.H., Johansson, A.V., 2005. Pressure statistics in high-Reynolds number turbulent boundary layer. TSFP DIGITAL LIBRARY ONLINE. Begel House Inc.

Tsuji, Y., Fransson, J.H., Alfredsson, P.H., Johansson, A.V., 2007. Pressure statistics and their scaling in high-Reynolds-number turbulent boundary layers. J. Fluid Mech. 585, 1–40.

Tsuji, Y., Imayama, S., Schlatter, P., Alfredsson, P.H., Johansson, A.V., Marusic, I., Hutchins, N., Monty, J., 2012. Pressure fluctuation in high-Reynolds-number turbulent boundary layer: results from experiments and DNS. J. Turbul (13), N50.

Tsuji, Y., Ishihara, T., 2003. Similarity scaling of pressure fluctuation in turbulence. Phys. Rev. E 68 (2), 026309.

Tsuji, Y., Marusic, I., Johansson, A.V., 2016. Amplitude modulation of pressure in turbulent boundary layer. Int. J. Heat Fluid Flow 61, 2–11.

Vedula, P., Yeung, P., 1999. Similarity scaling of acceleration and pressure statistics in numerical simulations of isotropic turbulence. Phys. Fluids 11 (5), 1208–1220.

Woodcock, J.D., Marusic, I., 2015. The statistical behaviour of attached eddies. Phys. Fluids 27 (1), 015104.

Yang, X.I.A., Abkar, M., 2018. A hierarchical random additive model for passive scalars in wall-bounded flows at high Reynolds numbers. J. Fluid Mech. 842, 354–380.

Yang, X.I.A., Marusic, I., Meneveau, C., 2016. Hierarchical random additive process and logarithmic scaling of generalized high order, two-point correlations in turbulent boundary layer flow. Phys. Rev. Fluids 1 (2), 024402.